Nano Research

Open Access

Research Article

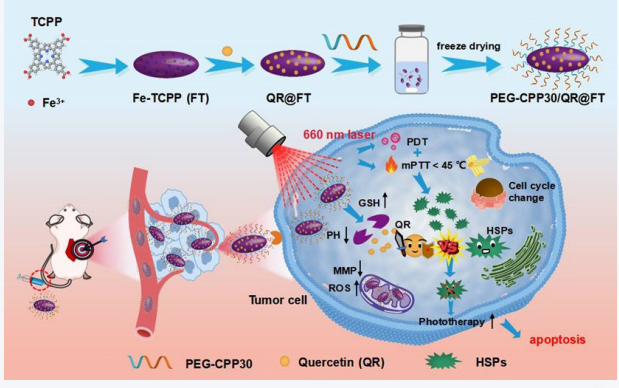
Anti-breast cancer effect of quercetin nanoparticles based on MOFs for chemo-phototherapy and heat shock proteins inhibition

Rongyue Zhu, Shilang Liao, Mengru Cai, Dongge Yin, Tingting Fu, Jing Liu, Yuji Du, Jiahui Kong, Rongrong Chang, Jian Ni ✉, and Xingbin Yin ✉

Beijing University of Chinese Medicine, Fangshan District, Beijing 102488, China

Cite this article: *Nano Research*, **2025**, *18*, 94906991. https://doi.org/10.26599/NR.2025.94906991

ABSTRACT: Phototherapy, including photodynamic therapy (PDT) and photothermal therapy (PTT), is a promising method of tumor treatment, which has the advantages of strong specificity and small side effects. However, PDT will aggravate the hypoxic environment in tumor cells, and PTT will lead to heat-resistant reaction, both of which will make the organism quickly produce heat shock proteins (HSPs) to protect itself, thus seriously hindering the therapeutic efficiency of phototherapy. As a natural HSPs inhibitor, quercetin (QR) provides a feasible way to solve this problem. Herein, a kind of metal organic framework (MOF), Fe-TCPP (FT), was used as a delivery material and photosensitizer to build a chemo-phototherapy platform, and QR was used as a chemotherapy drug and HSPs inhibitor. On this basis, the nanoparticles (NPs) were modified with PEG-CPP30 (a cell-penetrating peptide that specifically recognizes human breast cancer MCF-7 cells), which showed excellent targeting capacity and biocompatibility. The combination of chemotherapy and phototherapy significantly improved the anti-cancer effect. At the same time, NPs also showed prominent anti-HSPs effect. The effective connection of the two played a complementary role in the process of tumor treatment, which provided a new strategy for the accurate and efficient treatment of tumors in the future.



KEYWORDS: quercetin, Fe-metal organic frameworks (MOFs), phototherapy, anti-cancer, heat shock proteins inhibition

1 Introduction

Breast cancer refers to the uncontrolled proliferation of mammary epithelial cells under the action of a variety of carcinogenic factors, and is described as a heterogeneous disease [1]. As a member of the trio of formidable threats to women's health—alongside cervical and ovarian cancers—breast cancer looms as a significant peril to both longevity and well-being. According to the statistics of global cancer patients in 2020, among the 19.29 million new cases and 9.96 million deaths, the new incidence of breast cancer is 11.7%, surpassing even lung cancer and ranking first in the world. The death rate is 6.9%, the fourth highest in the world [2]. These figures starkly illuminate the profound impact of breast cancer on global health. At present, chemotherapy, surgery, radiotherapy, immunotherapy, phototherapy, etc. have been widely used in the treatment of cancer [3]. However, single-treatment modality is limited, with large side effects and strong harm. To navigate these challenges, combination therapies have emerged as a focal point for research and clinical exploration, holding promise for enhanced efficacy and reduced adverse effects.

Phototherapy stands as a promising avenue in tumor treatment, distinguished by its potent specificity and minimal side effects [4, 5]. Photodynamic therapy (PDT) operates by inducing reactive oxygen species (ROS) to eliminate tumor cells across a broader spectrum compared to chemodynamic therapy [6–9]. While photothermal therapy (PTT) utilizes localized high temperature to combat cancerous growth [10]. Compared with PTT, mild-temperature photothermal therapy (mPTT, < 45 °C) aims at treating cancer under a relatively low temperature [11], and has the advantages of high safety and few side effects on normal tissues [12]. However, PDT can induce oxidative stress in organisms and exacerbate the hypoxic microenvironment within tumors [13], while mPTT may provoke heat-resistant response in tumor cells [14]. Both scenarios

Received: February 22, 2024; **Revised:** May 29, 2024
Accepted: May 30, 2024

✉Address correspondence to Jian Ni, 602054@bucm.edu.cn; Xingbin Yin, yxbtcm@163.com

prompt rapid production of heat shock proteins (HSPs) as a protective mechanism [15]. When cells are exposed to extreme temperature, hypoxia, heavy metals and other environments, HSPs, as a kind of stress proteins widely existing in bacteria and mammals, play a role in maintaining the natural structure and function of cells [16, 17]. HSPs are closely related to the occurrence and development of tumor, and their high expression promotes the growth of tumor and hinders the therapeutic effect [18]. Therefore, solving the problem of HSPs response in phototherapy is the key to improve the anti-tumor effect. We decided to introduce a suitable HSPs inhibitor to solve this problem.

Quercetin (QR), a flavonol compound abundantly presenting in various medicinal plants like aster [19], spina gleditsiae [20], and notoginseng [21], exhibits diverse pharmacological activities. In recent years, QR has garnered increasing attention for its role in cancer therapy [22–24], functioning through the inhibition of cell proliferation and migration [25], promotion of tumor cell apoptosis [26], suppression of angiogenesis [27], and reversal of drug resistance [28]. Notably, QR possesses an additional attribute as a natural inhibitor of HSPs, rendering it an invaluable asset in cancer treatment [29, 30]. Integration of QR with phototherapy not only capitalizes on its anticancer properties but also addresses the challenge of HSPs response, thereby amplifying its anti-tumor efficacy. However, QR itself has the problems of poor water solubility [31] and low bio-availability [32], which seriously hinders the clinical application, so it is essential to adopt reasonable preparation means to improve its properties [33, 34].

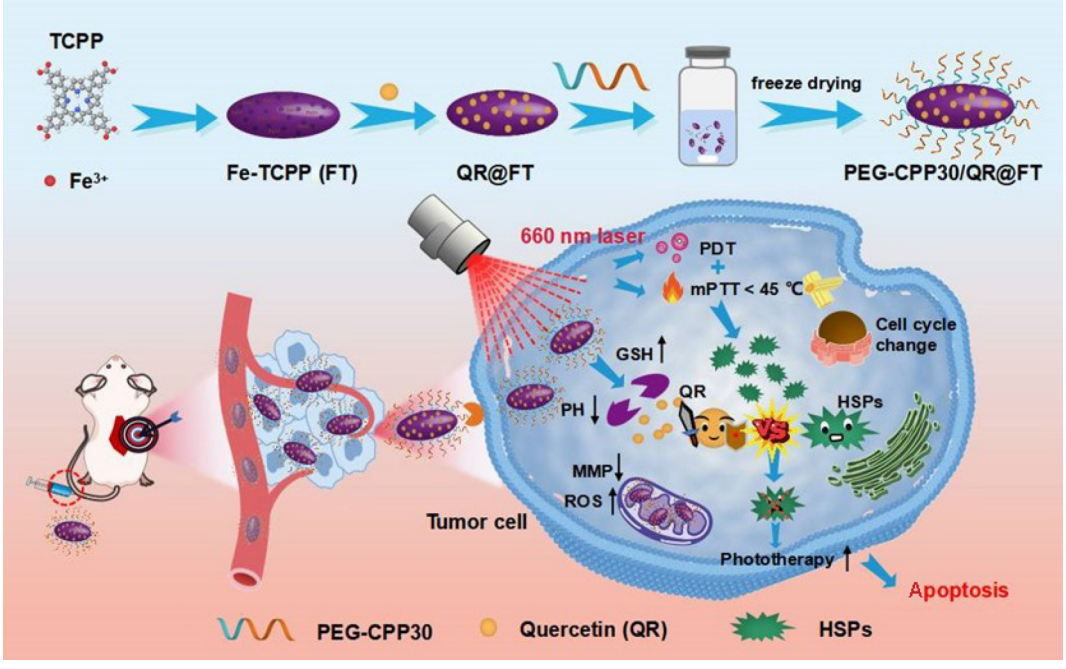
Metal organic frameworks (MOFs), a novel class of nanomaterials, initially found extensive utility in industrial sectors such as adsorption [35], gas storage [36], and catalysts [37], owing to their porous nature, large surface area, and abundant active sites. However, with advancements in technology leading to the gradual miniaturization of MOFs [38], coupled with their remarkable biocompatibility and facile modification [39, 40], these materials have found increasing application in various biomedical domains. At the same time, due to the adjustable of their structures [41], they provide convenient conditions for the introduction of photosensitizer. Fe-TCPP (FT) uses iron ion as metal ion and photosensitizer tetrad (4-carboxyphenyl) porphin (TCPP) as organic ligand directly with the advantages of good biocompatibility and high safety, which has been proved to be used for drug delivery [42]. Additionally, FT exhibits inherent photodynamic and photothermal properties, further enhancing its therapeutic potential.

In this study, we employed FT as a drug carrier and combined it with QR, a chemotherapy agent, and an HSPs inhibitor, to construct a synergistic chemo-phototherapy platform. To enhance the specificity of nanoparticles (NPs), we selected PEG-CPP30, a cell-penetrating peptide, as the surface modifier. Cell-penetrating peptides are a group of small polypeptides capable of traversing cell membranes without compromising membrane integrity. These peptides facilitate the intracellular uptake of nano-agents by tumor cells, thereby augmenting the efficacy of anti-cancer therapeutics. Specifically, CPP30 exhibits a selective affinity for MCF-7 human breast cancer cells [43, 44]. Leveraging this property, we engineered targeted NPs (PEG-CPP30/QR@FT) with superior drug loading capacity. MCF-7 cells served as the cellular model to assess the anti-breast cancer efficacy. Three representative heat shock proteins, HSP70, HSP90, and HSP27 [45–47], which are closely related to the development of tumor, were selected as indexes to evaluate the anti-HSPs effects of NPs, so as to realize the efficient integration of chemotherapy and phototherapy.

2 Results

2.1 Synthesis and characterization of FT

By heating magnetic stirring method, we successfully synthesized the FT material with suitable size. Scanning electron microscopy (SEM) results showed that FT was like-olivary (Fig. 1(a)) with a particle size of 240.40 ± 6.03 nm (Fig. S1 in the Electronic Supplementary Material (ESM)). The average zeta potential was 5.58 ± 2.41 mV, showing a positive charge (Fig. S4 in the ESM).



Scheme 1 Schematic of the chemo-phototherapy strategy of QR nanoparticle and its anti-cancer mechanism.

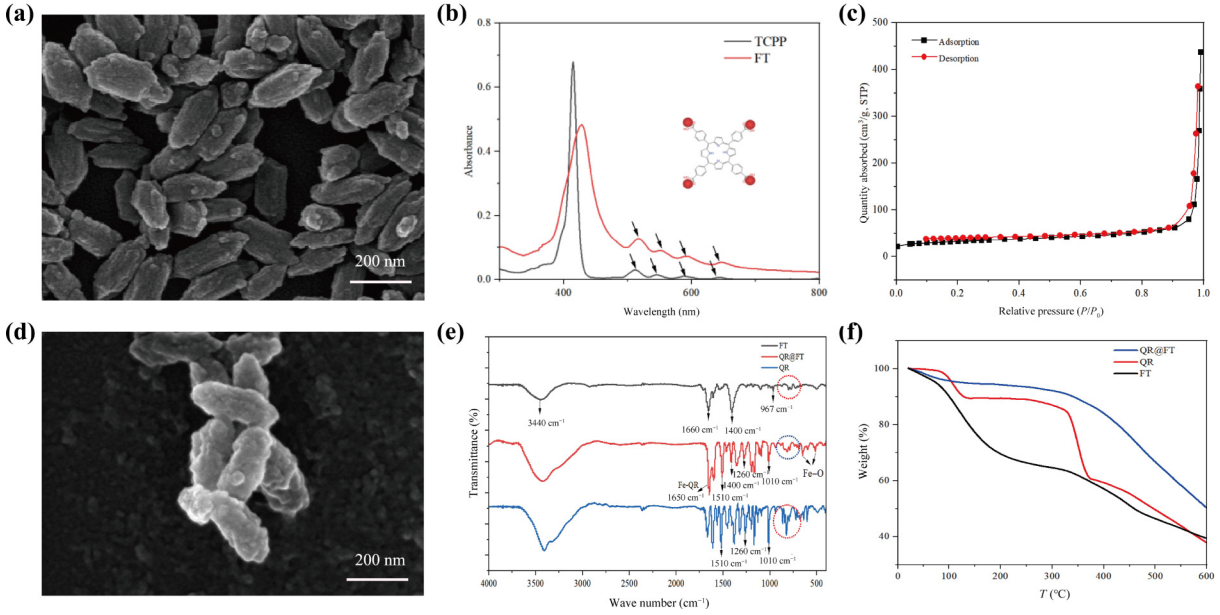


Figure 1 SEM of (a) FT and (d) QR@FT. (b) UV–vis spectrum of FT. (c) BET isotherm curves of FT. (e) FTIR spectrum of FT, QR, and QR@FT. (f) TGA curves of FT, QR, and QR@FT.

Ultra violet–visible (UV–vis) results (Fig. 1(b)) showed that both free TCPP and FT contain a major Soret peak and four Q-band peaks, so it can be seen that iron ion only binds to four carboxyl groups of TCPP instead of the central nitrogen atom. At the same time, compared with free TCPP, the Soret peak of FT had a certain degree of redshift, which also proved the introduction of Fe^{3+}. In Fourier transform infrared (FTIR) spectrum (Fig. 1(e)), the wide peak of 3600–3000 cm^{-1} was the characteristic absorption peak of –OH functional group, the stretching vibration of carboxylic acid carbonyl group at 1660 cm^{-1} ($\upsilon_{C=O}$), and the bending vibration of –OH in carboxylic acid at 1400 cm^{-1} (δ_{O-H}), which proved the existence of TCPP. The peak at 967 cm^{-1} was the out-of-plane bending vibration (γ_{N-H}) of TCPP amino group, which was consistent with the results of UV–vis. The stretching vibration at 910–665 cm^{-1} proved the existence of benzene ring skeleton. Brunauere Emmette Teller (BET) curve (Fig. 1(c)) showed that FT was a mesoporous material with a specific surface area of 116.93 m^2/g, a pore volume of 0.65 cm^3/g and a pore size of 22.20 nm.

2.2 Drug loading and characterization of QR@FT

Through orthogonal test process optimization, the optimal drug loading process was determined. The loading time was 3 days, drug-to-carrier ratio was 3:1 and the drug concentration was 8 mg/mL. The drug-loading capacity of QR@FT NPs can reach 54.90 wt.% ± 1.39 wt.%. Three batches of verification experiments confirmed that the drug-loading process was repeatable and feasible (Tables S2–S4 in the ESM).

SEM results showed that the shape of QR@FT did not change after the QR was loaded (Fig. 1(d)), with a slightly larger particle size of 295.37 ± 4.48 nm (Fig. S2 in the ESM). The Zeta potential of the QR@FT was flipped, the average value was −7.04 ± 0.65 mV (Fig. S4 in the ESM). The FTIR characteristic peaks of both FT and QR appeared in the spectra of QR@FT (Fig. 1(e)). In the fingerprint section, a peak similar to FT (stretching vibration of the benzene ring skeleton) appeared, but the QR absorption peak in this section disappeared. Compared with FT, the characteristic peak of QR benzene ring skeleton vibration appeared at 1510 cm^{-1} in the spectrum of QR@FT. The stretching vibration peak of C–O appeared at 1010 cm^{-1} (υ_{C-O}). At 1260 cm^{-1}, an in-plane swing peak of the carbonyl group of unsaturated ketone appeared, and similar peaks existed in the spectrum of QR. In addition, Fe–O coordination peaks appeared at 1650, 512 and 648 cm^{-1} which may be formed by the coordination of Fe^{3+} with QR's phenolic hydroxyl group. The results showed that FT and QR were successfully combined. Thermogravimetric analyzer (TGA) results (Fig. 1(f)) showed that FT had a certain thermal sensitivity when exposed to high temperature, this may be due to the photothermal performance of TCPP. However, when combined with QR, the thermal stability of the NPs increased. Among the three NPs, QR@FT had the best thermal stability.

2.3 Synthesis and characterization of PEG-CPP30/QR@FT

Targeted NPs, PEG-CPP30/QR@FT were successfully prepared by reaction coating method. SEM images (Fig. 2(a)) showed that the particles seemed to be coated with a layer of jelly compared with QR@FT, indicating that the peptide was successfully modified on the surface of QR@FT. The particle size of PEG-CPP30/QR@FT was further increased to 336.57 ± 4.92 nm (Fig. S3 in the ESM). The Zeta potential of the modified NPs was further deflected towards the negative potential, with an average value of −12.40 ± 0.17 mV (Fig. S4 in the ESM). Compared with QR@FT, the FTIR characteristic peak (Fig. 2(b)) of PEG-CPP30/QR@FT's benzene ring vibration at 900–500 cm^{-1} disappeared, and the resulting peak was similar to that of PEG-CPP30, which may be due to the coating of transmembrane peptide covering the benzene ring vibration peak. Moreover, the spectrum of PEG-CPP30/QR@FT showed a characteristic peak of PEG-CPP30 at 1630 cm^{-1}. It can be seen that PEG-CPP30/QR@FT was successfully synthesized.

2.4 Photodynamic and photothermal properties of PEG-CPP30/QR@FT

FT, QR@FT and PEG-CPP30/QR@FT all have certain photodynamic and photothermal conversion properties. In terms of photodynamic property, we used 1,3-Diphenylisobenzofuran (DPBF) as singlet oxygen trapping agent, and measured the residual

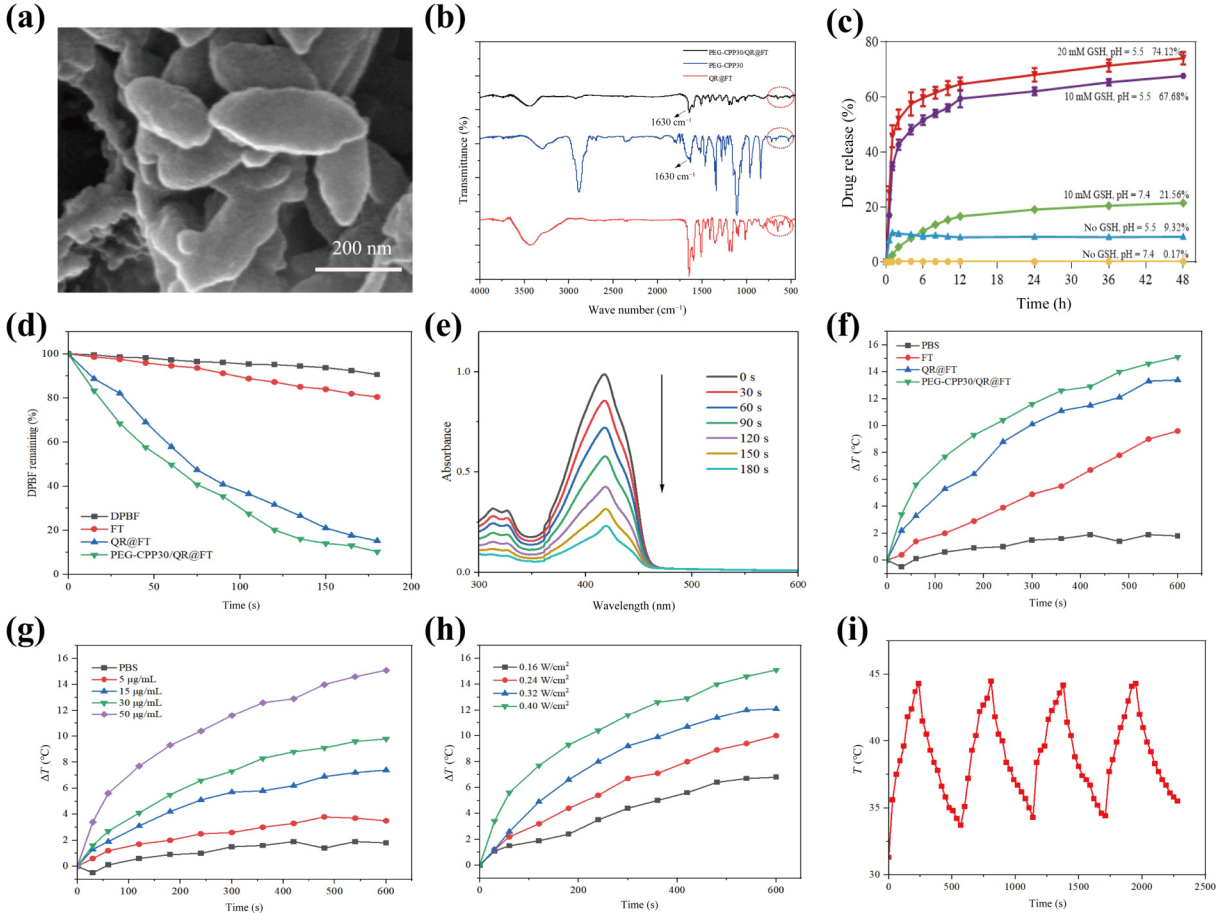


Figure 2 (a) SEM image of PEG-CPP30/QR@FT. (b) FTIR spectrum of QR@FT, PEG-CPP30, and PEG-CPP30/QR@FT. (c) Release curves of PEG-CPP30/QR@FT in different conditions. (d) The DPBF remaining curves and (e) the full-band UV–vis spectrogram for evaluating singlet oxygen generation capacity of NPs. (f) *In vitro* temperature rise curve of different NPs. (g)–(h) *In vitro* temperature rise curve of PEG-CPP30/QR@FT under different concentrations and irradiation powers. (i) Irradiation cycle curve of PEG-CPP30/QR@FT.

amount of DPBF by the change of UV–vis absorbance at different time points after laser irradiation (Figs. 2(d) and 2(e)). The experimental results showed that after laser irradiation, NPs (50 μg/mL) can produce a large amount of singlet oxygen, which gradually reduced the content of DPBF, showing good photodynamic properties. In terms of photothermal property, PEG-CPP30/QR@FT had the best photothermal performance (Fig. 2(f)). When the irradiation power is constant, the photothermal property of PEG-CPP30/QR@FT was concentration-dependent (Fig. 2(g)), power-dependent (Fig. 2(h)), and time-dependent. With the increase of the number of laser cycles, the maximum temperature of PEG-CPP30/QR@FT NPs could always be maintained at about 44 °C (Fig. 2(i)), which proved that PEG-CPP30/QR@FT had good photothermal stability and met the temperature range of mPTT.

2.5 *In vitro* drug release investigation

We investigated the release conditions of PEG-CPP30/QR@FT under different pH and glutathione (GSH) concentrations. We set up 5 kinds of release environments (base releasing medium was PBS solution containing 0.5% Tween-80), respectively: 0 mM GSH/pH = 7.4, 0 mM GSH/pH = 5.5, 10 mM GSH/pH = 7.4, 10 mM GSH/pH = 5.5, and 20 mM GSH/pH = 5.5. The release curves showed that PEG-CPP30/QR@FT had dual pH/GSH response release characteristics (Fig. 2(c)). When the concentration of GSH was 0 mM and the pH was 7.4, the NPs almost didn't release. When the pH reduced to 5.5, the NPs began to release, but with release rate of only 9.32% within 48 h. When GSH existed in the environment, the NPs began to release in large quantities, the release rates were 21.56% (10 mM GSH/pH = 7.4) and 67.68% (10 mM GSH/pH = 5.5), respectively. When the concentration of GSH raised to 20 mM (pH = 5.5), the release rate of NPs could increase to 74.12%. In conclusion, under the dual conditions of low pH and the presence of GSH, a large amount of drug release would be triggered, and the redox response mediated by GSH was concentration-dependent.

2.6 Cell targeting selectivity and uptake

As shown in the Figs. 3(a)–3(c), Cou6 and Cou6@FT exhibited obvious green fluorescence in all four kinds of cells, which indicated that their selectivity was not enough and damage might be caused to normal tissues. However, PEG-CPP30/Cou6@FT showed obvious and strong green fluorescence only when it acted on MCF-7 cells. These results indicated that the NPs modified by PEG-CPP30 had active targeting performance and obvious characteristics of MCF-7 cells selection. Flow cytometry results (Fig. 3(d)) showed that MCF-7 had the strongest uptake capacity to PEG-CPP30/Cou6@FT. The first reason was that FT increased the passive targeting ability of the drug, the second reason was that NPs coated with cell-penetrating peptides could be easily internalized by tumor cells through the endocytosis (including macropinocytosis,

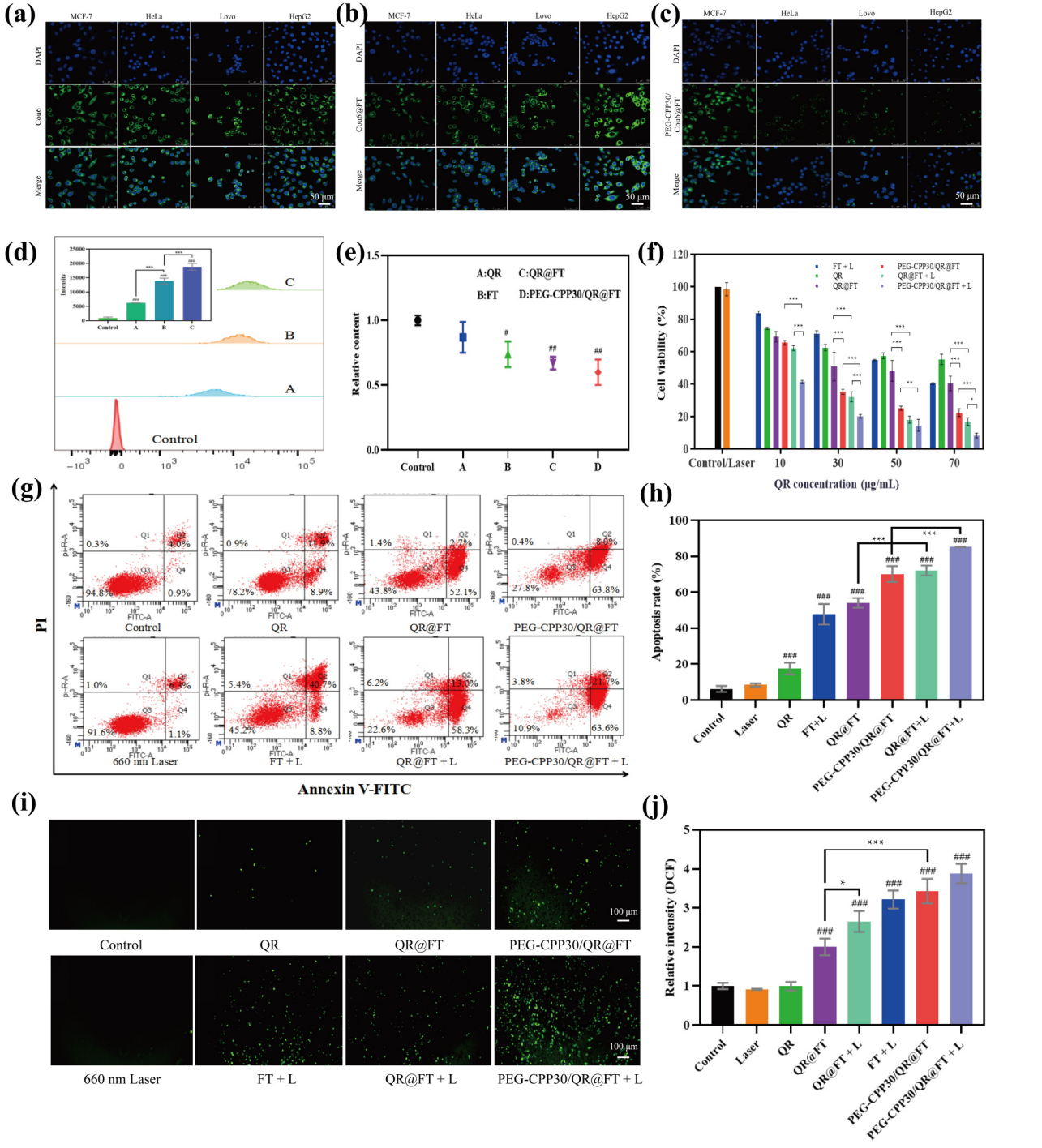


Figure 3 Confocal laser scanning microscopy (CLSM) images of (a) Cou6, (b) Cou6@FT, and (c) PEG-CPP30/Cou6@FT in four kinds of cells. Scale bars: 50 μm. (d) Flow cytometry results of uptake of NPs by MCF-7 cells. (e) GSH content of MCF-7 cells measured by GSH assay kit. (f) Cell viability of MCF-7 cells treated with NPs. (g) Flow cytometry analysis of MCF-7 cells treated with NPs and (h) the statistical apoptosis rate. (i) Fluorescence microscope images of MCF-7 cells treated with NPs (DCFH-DA staining) and (j) the statistical ROS change. Scale bars: 100 μm. $^{*}P < 0.05$, $^{**}P < 0.01$, $^{***}P < 0.001$, compared between two groups; $^{\#}P < 0.05$, $^{\#\#}P < 0.01$, $^{\#\#\#}P < 0.001$, compared to control group.

caveolin-mediated endocytosis, clathrin-mediated endocytosis, and clathrin and caveolin-independent endocytosis) [48], which also verified that CPP30 transmembrane peptide can target MCF-7 cells [43].

2.7 *In vitro* cell efficacy evaluation

Tumor cells contain high levels of GSH. From the above drug release results, it could be seen that high content of GSH will cause the collapse of the FT material skeleton, so as to achieve the release of drugs to make NPs work. In order to verify whether the NPs can consume high levels of GSH in tumor cells, we performed a GSH detection (Fig. 3(e)). The results showed that after treatment, the intracellular GSH content decreased significantly, and PEG-CPP30/QR@FT had the strongest effect, which suggested that NPs could play a role by consuming intracellular GSH, promoting the release of the drug.

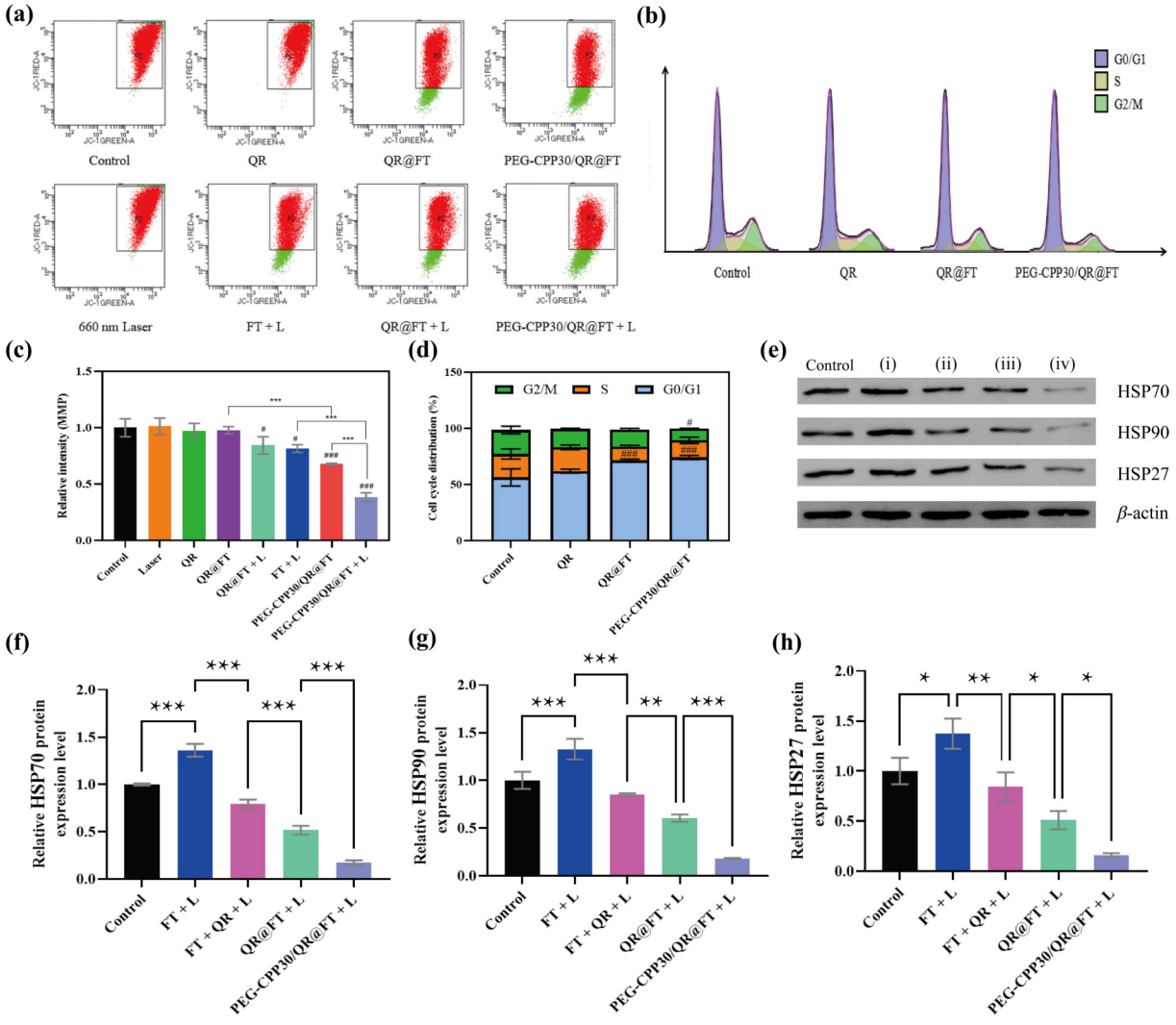


Figure 4 (a) Flow cytometry detection and (c) the statistical analysis of MMP change of MCF-7 cells treated with NPs (JC-1 staining). (b) Flow cytometry detection and (d) the statistical analysis of cell cycle change of MCF-7 cells treated with NPs (PI staining). (e) Expressions of HSP70, HSP90, HSP27 in MCF-7 cells treated with NPs: (i) FT + L group; (ii) FT + QR + L group; (iii) QR@FT + L group; (iv) PEG-CPP30/QR@FT + L group. Relative protein expression of (f) HSP70, (g) HSP90, and (h) HSP27. $^{*}P < 0.05$, $^{**}P < 0.01$, $^{***}P < 0.001$, compared between any two groups; $^{\#}P < 0.05$, $^{\#\#}P < 0.01$, $^{\#\#\#}P < 0.001$, compared to control group.

3-(4,5-Dimethylthiazol-2-yl)-2,5-diphenyltetrazolium bromide (MTT) and 4',6-Diamidino-2'-phenylindole (DAPI) assays were used to evaluate the safety of blank material FT (Figs. S5 and S6 in the ESM). The experimental results showed that 0–100 μg/mL FT had good safety, which showed that the blank material was safe and with low toxicity.

The inhibitory effect of different concentrations and preparations on MCF-7 cells was determined by MTT assay (Fig. 3(f)). The results showed that the cytotoxicity of MCF-7 cells in each administration group was dose-dependent. PEG-CPP30/QR@FT exhibits the strongest pharmacodynamic effect regardless of laser exposure. This was because the modification of PEG-CPP30 enhanced the endocytogenic uptake of drugs by tumor cells which improved the efficacy of chemotherapy. After laser irradiation, the therapeutic effect was significantly improved. The inhibition rate of PEG-CPP30/QR@FT + L group (QR concentration: 70 μg/mL) reached 91.11%, which was much higher than 44.71% of free QR and 59.65% of FT + L group. It could be seen that the combined treatment of chemo-phototherapy is superior to monotherapy, achieving the purpose of combined treatment. The results of DAPI experiment proved that MCF-7 cells showed nucleolysis after administration, especially after laser exposure (Fig. S7 in the ESM). The results of apoptosis experiment (Figs. 3(g) and 3(h)) were consistent with MTT assay. PEG-CPP30/QR@FT + L showed the best pro-apoptotic effect. After irradiation, the pro-apoptotic effect was more obvious in all groups. The percentage of apoptosis in PEG-CPP30/QR@FT + L group (QR concentration: 50 μg/mL) reached 85.23%, which was much higher than that in the other groups.

In order to explore the anti-tumor mechanism of NPs, fluorescence microscopy and flow cytometry were used to measure the changes of ROS, mitochondrial membrane potential (MMP) and cell cycle. When ROS existed, non-fluorescent 2',7'-dichlorofluorescin diacetate (DCFH-DA) would be transformed into the fluorescent 2',7'-dichloro-fluorescein (DCF) [49]. The experimental results showed that the content of ROS increased to varying degrees after treatment, and more significantly after laser irradiation (Figs. 3(i) and 3(j), and Fig. S8 in the ESM). This suggested that NPs could play an anti-tumor role by promoting the production of ROS. The changes of MMP were determined using

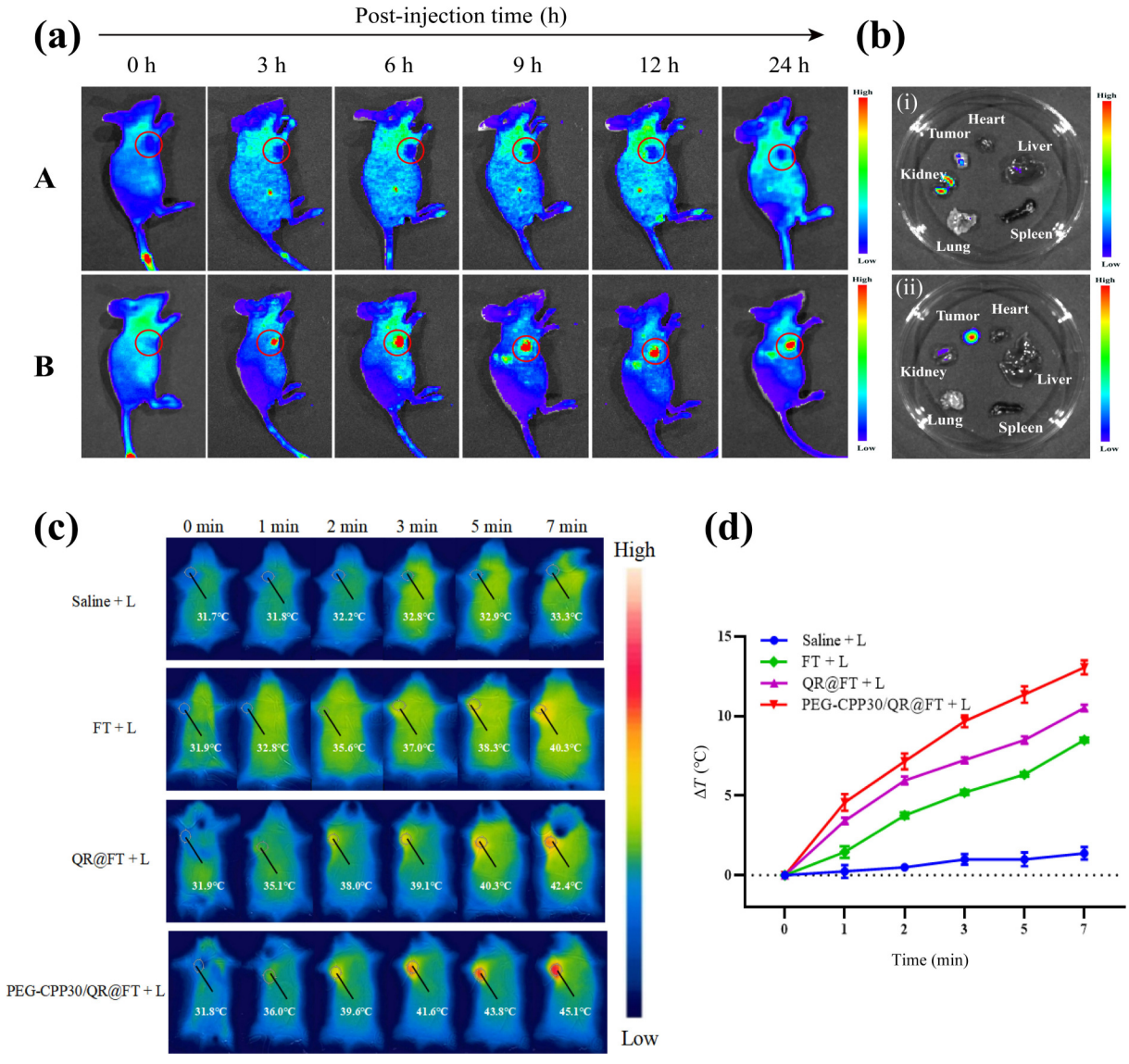


Figure 5 (a) The *in vivo* fluorescence images of tumor-bearing mice at different time points after the i.v. injection of NPs (n = 3). (b) The *in vitro* fluorescence images of tumors and major organs of mice treated with NPs. (i) Sodium fluorescein-labeled FT group; (ii) sodium fluorescein-labeled PEG-CPP30/FT group. (c) Infrared thermal images of tumor-bearing mice during laser irradiation and (d) heating curves at the tumor sites after the i.v. injection of saline, FT, QR@FT, and PEG-CPP30/QR@FT (0.4 W/cm^2 for 0, 1, 2, 3, 5, and 7 min, n = 5).

JC-1 as fluorescent dye. When the MMP was high, JC-1 was a polymer showing red fluorescence. Conversely, JC-1 was a monomer showing green fluorescence (Fig. S9 in the ESM) [50]. The experimental results showed that (Figs. 4(a) and 4(c)) the relative value of MMP was decreased after the treatment of NPs, which proved that the NPs could promote the apoptosis of tumor cells by influencing mitochondria. Cell cycle results showed that (Figs. 4(b) and 4(d), and Fig. S10 in the ESM) NPs could act by blocking the G0/G1 phase of cell proliferation.

2.8 HSP70, HSP90, and HSP27 measurement by western blot

Three HSPs (HSP70, HSP90 and HSP27) were selected as indicators to evaluate the anti-HSPs effect of NPs. The results showed that when the cells were treated with phototherapy (FT + L group), the expression of the three HSPs increased apparently (Figs. 4(e)–4(h)). When QR was present in the treatment environment, the expression of HSPs decreased to different degrees, and the effect of QR-loaded particles was better than that of free QR. In particular, PEG-CPP30/QR@FT showed the strongest anti-HSPs expression capacity. This fully showed that our idea of combining QR (HSPs inhibitor) with phototherapy is feasible, and this combination treatment effectively solved the core problem of HSPs response in phototherapy.

2.9 *In vivo* bio-distribution and photothermal conversion effect study

We constructed a tumor-bearing mouse model of MCF-7. After injecting different NPs labeled with sodium fluorescein into tumor-bearing mice, fluorescence imaging was performed *in vivo* at different time points within 24 h. The experimental results showed that the targeted NPs had gathered at the tumor site within 3 h, and the fluorescence signal was still present at 24 h. However, the non-targeted NPs failed to achieve significant aggregation at the tumor

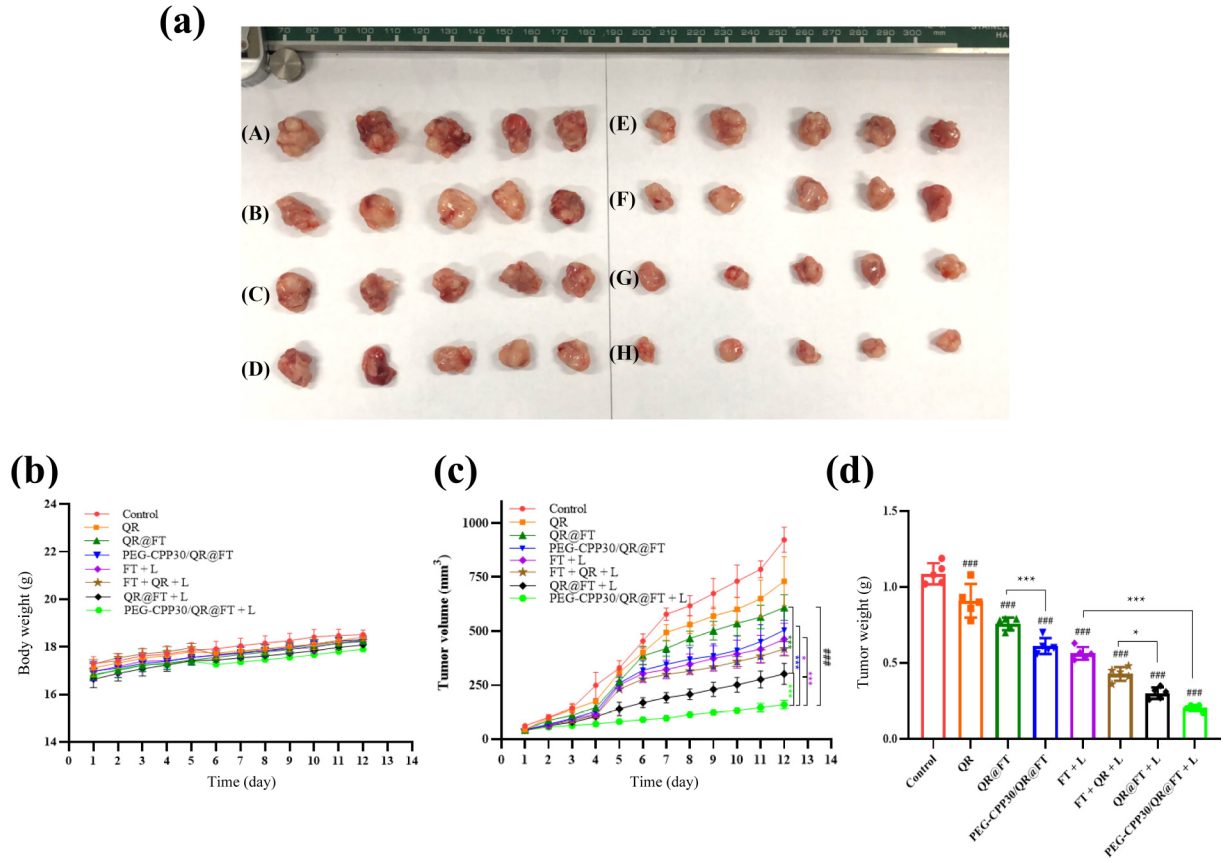


Figure 6 (a) Images of tumor tissues. (A) Control group; (B) QR group; (C) QR@FT group; (D) PEG-CPP30/QR@FT group; (E) FT + L group; (F) FT + QR + L group; (G) QR@FT + L group; (H) PEG-CPP30/QR@FT + L group. *In vivo* antitumor effect on the MCF-7 tumor-bearing mice treated with different NPs (n = 5): changes of (b) body weight, (c) tumor volume in mice during treatment, and (d) weights of tumor tissues *in vitro* after treatment.

site within 24 h, indicating that the targeting capacity of NPs was significantly improved after modification with PEG-CPP30 (Fig. 5(a), and Fig. S11 in the ESM). After 9 h of injection, targeted NPs accumulated the most at the tumor site (Fig. S11(a) in the ESM). Therefore, in the following *in vivo* pharmacodynamics experiments, we chose to perform laser irradiation on the tumor site of mice at 9 h after tail vein injection to ensure the best therapeutic effect. After 24 h of injection, the mice were killed, the tumors and major organs were dissected. We found that the non-targeted NPs mainly gathered in the kidney and liver of the mice, and a small amount gathered in the tumor sites. However, the targeted NPs could accumulate in large quantities at the tumor sites, which further proved the good targeting capacity of NPs (Fig. 5(b), and Fig. S11(b) in the ESM).

The results of *in vivo* photothermal conversion experiments showed that the FT, QR@FT and PEG-CPP30/QR@FT could realize photothermal conversion *in vivo*. Among them, PEG-CPP30/QR@FT had the best photothermal performance at the same condition. After 3 min of irradiation, the temperature of tumor site in mice increased to 41.6 °C, reaching the standard of mPTT. After 7 min of irradiation, the tumor site increased by about 13 °C, showing significant difference compared with saline group (Figs. 5(c) and 5(d)).

2.10 *In vivo* anti-tumor effect evaluation

In order to better explore the anti-tumor activity of NPs, we conducted a series of *in vivo* pharmacodynamics experiments. After successful modeling, the drug was administered every other day (with QR content of 8 mg/kg) throughout the treatment cycle, the weight and tumor size were weighed every day. The experiment results showed that there was no significant difference between the weight of mice in each group (Fig. 6(b)), which proved that the NPs had good biocompatibility and did not cause significant harm to mice generally. The tumor suppression experiment results (Fig. 6(c)) showed that, compared with the control group, the tumor growth of mice treated with NPs was inhibited to varying degrees, the targeted preparation group was better than the non-targeted preparation group, and the illuminated group was better than the unilluminated group. After the mice were euthanized, the tumors were weighed. The experimental results (Figs. 6(a) and 6(d), and Fig. S12 in the ESM) showed that the average tumor weight of the control group was 1.09 ± 0.07 g, while that of the PEG-CPP30/QR@FT + L group was only 0.20 ± 0.02 g, which was the lowest and significantly different from that of the control group. On the one hand, the transmembrane peptide of CPP30 enhanced the uptake of NPs by tumor cells, and on the other hand, the combination of chemotherapy and phototherapy was superior to chemotherapy alone or phototherapy alone, achieving the purpose of combined therapy.

After 12 days of administration, the mice were euthanized, tumor sites and major organs were dissected, and hematoxylin & eosin (H&E) staining was performed (Fig. 7). The results of H&E pathological sections showed that tumor cells in the control group were dense and deeply stained, while after administration and laser treatment, tumor cells in the tumor sites were loose and a large number of tumor nuclei were reduced or disappeared, especially in

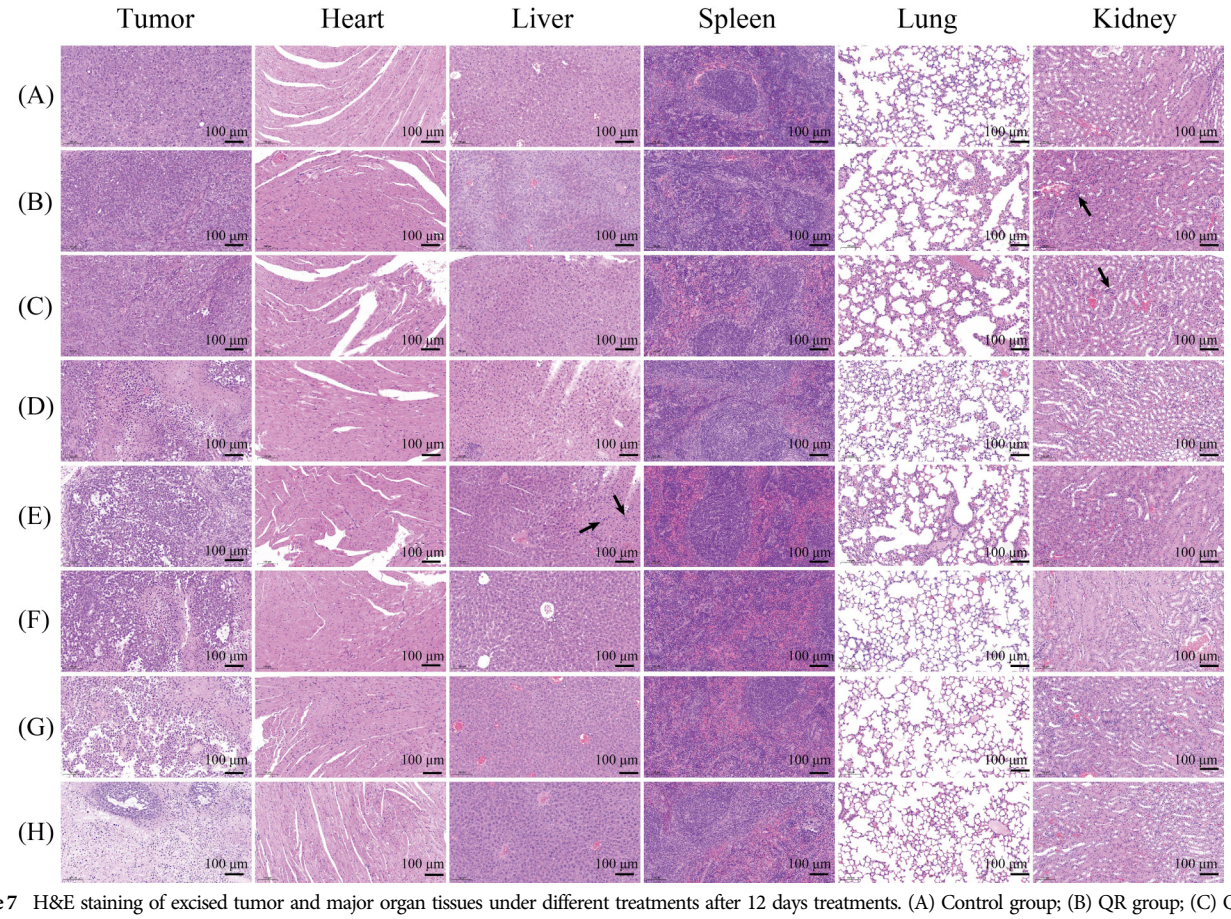


Figure 7 H&E staining of excised tumor and major organ tissues under different treatments after 12 days treatments. (A) Control group; (B) QR group; (C) QR@FT group; (D) PEG-CPP30/QR@FT group; (E) FT + L group; (F) FT + QR + L group; (G) QR@FT + L group; (H) PEG-CPP30/QR@FT + L group, scale bars: 100 μm.

PEG-CPP30/QR@FT + L group. This indicated that the NPs had strong antitumor activity. Sections of the organ tissues showed that QR, FT, and QR@FT without PEG-CPP30 modification would cause minor damage to the liver and kidney. Nucleolysis was observed locally in the liver section, and slight inflammatory infiltration was observed locally in the kidney section (arrow pointing). In contrast, PEG-CPP30-modified NPs did not cause significant damage to any organs. This showed that the modified NPs exhibited stronger biosecurity. Overall, none of the NPs in each group caused serious organ damage in mice, the cell outline and structure was clear, demonstrating that our NPs were safe and biocompatible.

To further confirm that the NPs had good anti-HSPs effects. We selected tumor tissues of control, FT + L, FT + QR + L, QR@FT + L, and PEG-CPP30/QR@FT + L groups for immunofluorescence determination of HSP70, HSP90, and HSP27 (Fig. 8). The results showed that three HSPs in FT + L group were significantly increased. After QR was added, the production of three HSPs in FT + QR + L group, QR@FT + L group, and PEG-CPP30/QR@FT + L group were inhibited to varying degrees. The inhibition effect of PEG-CPP30/QR@FT + L group was the most prominent. This showed that NPs can indeed effectively inhibit the production of HSPs in phototherapy, and after targeted modification, more NPs could be taken up by tumor cells, so PEG-CPP30/QR@FT showed the best HSPs inhibition effect. This further indicated that our experimental design was effective and feasible, which not only played an anti-tumor role, but also solved the problem of HSPs response in phototherapy.

3 Conclusions and discussion

3.1 Conclusions

In this study, based on the purpose of combination of chemotherapy and phototherapy, we prepared a kind of targeted drug-carrying nanoparticle PEG-CPP30/QR@FT, modified by cell membrane transmembrane peptide, with a drug loading of up to 54.90%. *In vivo* and *in vitro* experiments showed that the NPs had good biocompatibility and targeting capacity, which could exert anti-tumor effect by promoting apoptosis, promoting ROS production, reducing MMP, regulating cell cycle and so on. The material FT provided a phototherapy platform, QR not only played an anti-tumor role, but also acted as an HSPs inhibitor. QR itself had limited anti-tumor effect, but the effect of the NPs was significantly improved after combined therapy. At the same time, QR also solved the problem of HSPs response in phototherapy. Two kinds of treatment complemented and promoted each other, and finally realized the efficient treatment effect. This study provided a new idea and a new possibility for the future construction of nano platform for chemo-phototherapy.

3.2 Discussion

TCPP possesses inherent photodynamic and photothermal properties. However, its propensity for aggregation and quenching poses challenges in its direct application. Consequently, in most studies, TCPP serves as an organic ligand complexed with metal ions to form MOFs [51, 52]. This approach not only enhances

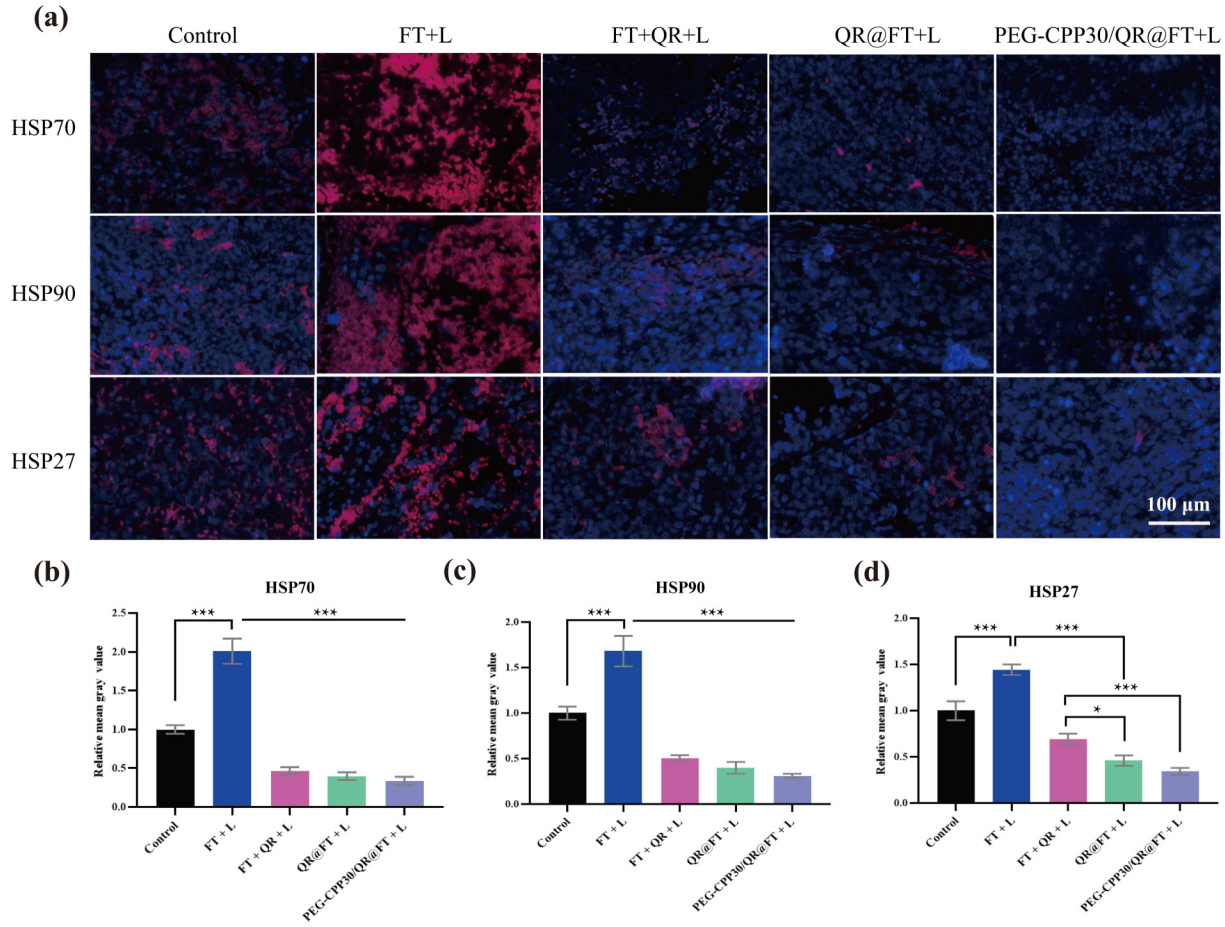


Figure 8 (a) Immunofluorescence images of tumor tissues showed the expression of HSP70, HSP90, HSP27 under different treatments (blue: cell nuclei; red: HSPs). Fluorescence intensity of (b) HSP70, (c) HSP90, and (d) HSP27 under different treatments. $^{*}P < 0.05$, $^{**}P < 0.01$, $^{***}P < 0.001$, compared between any two groups.

TCPP's dispersibility and stability, but also mitigates issues of aggregation and fluorescence quenching. Among metal options, iron stands out as an essential trace element in the human body, endowing iron-containing MOFs with a high safety profile [53]. Moreover, iron ions readily react with excess GSH and hydrogen peroxide (H_2O_2) within tumor cells, conferring pH and GSH-responsive characteristics to the nanomaterial [54, 55]. This property facilitates targeted drug release within the tumor microenvironment. Furthermore, the Fenton reaction catalyzed by iron ions generates oxygen, augmenting the efficiency of phototherapy [56, 57], a capability not intrinsic to TCPP alone. Additionally, TCPP lacks direct drug-loading capacity and tumor-targeting specificity. However, upon combination with iron ions to form MOFs, the resulting material becomes porous, allowing for drug encapsulation (e.g., quercetin). Moreover, MOFs exhibit facile surface modification capabilities, enabling the attachment of various targeting moieties [58] via straightforward reactive coating methods, thereby imparting active tumor-targeting properties. In a word, TCPP imparts good optical properties to FT, and the addition of iron ions also adds new properties to TCPP, and effectively improves the defects of TCPP. So we finally choose Fe-TCPP with better performance as a nanomaterial for follow-up experimental exploration.

Given FT's dual pH/GSH responsiveness, we conducted an investigation into its remaining species under relevant conditions. Our findings revealed that FT underwent degradation, yielding free Fe^{2+} and TCPP. Initially, we examined the change of iron ions within the material using *o*-phenanthroline as an iron ion indicator [55]. This compound forms an orange complex with Fe^{2+} and a colorless complex with Fe^{3+}. To elucidate the process, we incubated FT with excess GSH (100 mM) under acidic conditions. Subsequent analysis confirmed the reduction of Fe^{3+} to Fe^{2+}, as evidenced by the orange coloration observed in the FT + GSH group solution post-incubation (Fig. S13 in the ESM). Next, we examined the release of TCPP in FT. The experimental results showed that under the condition of pH = 5.5 and GSH = 20 mM, the cumulative release rate of TCPP can reach 70.9% within 60 h (Fig. S14(a) in the ESM). Meanwhile, the UV–vis spectrum of 300–800 nm proved that the Soret peak of material FT showed an obvious redshift phenomenon compared with TCPP. After the release, the Soret peak of FT returned to the original wavelength (Fig. S14(b) in the ESM). The above results proved that TCPP was indeed released from FT material after incubation, and FT degraded into free Fe^{3+} and TCPP at low pH and a certain concentration of GSH.

4 Experimental

4.1 Materials and reagents

$FeCl_3{\cdot}6H_2O$, TCPP, benzoic acid and quercetin (≥ 97%) were supplied by Shanghai Yuanye Bio-Technology Co., Ltd. N,N-dimethylformamide (DMF, 99.5%) was purchased from Tianjin Zhiyuan Chemical reagent Co., Ltd. DPBF was supplied by Beijing

Suolaibao Technology Co., Ltd. High-glucose Dulbecco's modified eagle medium (DMEM) was supplied by Sigma. Fetal bovine serum (FBS) was supplied by Beijing Sijiqing Bio-Technology Co., Ltd.. Phosphate buffered saline (PBS) was supplied by Thermo Fisher Scientific Technology Co., Ltd.. Trypsin was obtained from Gibco. MTT was furnished from Beijing Biodee Biotechnology Co., Ltd. DAPI dye, GSH detection kit, Annexin V-FITC apoptosis detection kit, reactive oxygen species detection kit, mitochondrial membrane potential detection kit (JC-1) and cell cycle detection kit were purchased from Shanghai Beyotime Biotechnology Co., Ltd. Primary antibodies beta-actin, HSP27, HSP70, HSP90 were obtained from Abcam, UK.

4.2 Synthesis of PEG-CPP30/QR@FT

4.2.1 Synthesis of FT

$FeCl_3{\cdot}6H_2O$ (30 mg, 2 mL), TCPP (10 mg, 4 mL) and benzoic acid solution (280 mg, 4 mL) were dissolved with DMF, respectively. The mixture of three prepared solutions were continuously stirred at a speed of 800 rpm at 90 °C for 5 h, and centrifuged subsequently. The product was washed with DMF for 3 times, and dried at 60 °C in a vacuum drying oven for 24 h. The synthesized sample as dry purplish-red powder solid was obtained [59].

4.2.2 Synthesis of QR@FT

The optimal loading process of FT for QR was selected by orthogonal experiment (Table S1 in the ESM). In brief, under the condition of avoiding light, a certain amount of FT and QR were stirred in methanol at a speed of 600 rpm. After the preparation, QR@FT were washed with methanol and dried at 60 °C. Drug loading capacity was determined by high performance liquid chromatography (HPLC) and calculated according to formula S1 in the ESM.

4.2.3 Synthesis of PEG-CPP30/QR@FT

QR@FT and PEG-CPP30 (the mass ratio is 5:1) were evenly mixed in purified water and stirred at a speed of 600 rpm for 1 h at room temperature. The product PEG-CPP30/QR@FT obtained was centrifuged and freeze-dried.

4.3 Characterization

The morphology and structure of the NPs were characterized by SEM (Hitachi S-4700, Japan). The size and Zeta potential of the NPs were determined by a Malvern nanometer particle size analyzer (Malvern Nano Zetasizer S90, Malvern, UK). The characteristic peaks of NPs were measured by FTIR (Thermo Fisher Nicoler-6700, USA). The special functional groups of NPs were determined by ultraviolet and visible spectrophotometry (UV–vis, TU-1810PC, China). The thermal stability of NPs was measured by a TGA (Q5000IR, China). The pore size of the NPs was determined by a BET sorptometer (Bel Japan Inc., Japan).

4.4 Photodynamic and photothermal properties of NPs *in vitro*

We used DPBF as singlet oxygen trapping agent to evaluate the photodynamic capacity *in vitro*. In the experiment, 4×10^{-5} mol/L DPBF solution was put into a quartz plate, and 50 μg/mL FT, QR@FT, PEG-CPP30/QR@FT (with 50 μg/mL QR content) were added. The absorbance was measured every 15 s of laser irradiation, and the UV–vis spectrum were scanned every 30 s of laser irradiation. The ability of NPs to produce singlet oxygen was evaluated by the change of absorbance. In order to investigate the photothermal conversion performance of the NPs, we dissolved the NPs (FT, QR@FT, PEG-CPP30/QR@FT) in PBS (the concentration is consistent with the photodynamic experiment), plotted the temperature rise curves under the 0.4 W/cm^2 660 nm laser irradiation. At the same time, we explored the photothermal effect of PEG-CPP30/QR@FT under different concentrations and irradiation powers within 10 min, and investigated its photothermal stability.

4.5 *In vitro* drug release investigation

The release behavior of targeted NPs *in vitro* was investigated by centrifugal method. In addition to being affected by pH, FT contains Fe^{3+} can undergo redox reaction with higher concentration of GSH [48] in tumor cells to produce Fe^{2+} and finally lead to the collapse of FT skeleton, thus achieving the release of QR. In the release experiments, the effects of different pH and concentration of GSH on the release performance of targeted NPs were investigated respectively (the release medium is 0.5% Tween-80). The cumulative release rate was calculated using formula S2 in the ESM.

4.6 Cell targeting selectivity and uptake detection

MCF-7, HeLa, Lovo and HepG2 cells were incubated in a laser confocal dish (15×10^4 cells per well). After overnight culture, the medium was removed. 1 mL medium containing Cou6, Cou6@FT, and PEG-CPP30/Cou6@FT (with 0.5 μg/mL Cou6 content) was added. After administration for 4 h, the cells were washed by PBS, stained by DAPI, and finally photographed by confocal laser scanning microscopy (CLSM). The uptake condition of different NPs by MCF-7 cells was measured by flow cytometry (FACSCanto II, USA).

4.7 *In vitro* cytotoxicity test

MTT assay was used to determine cytotoxicity *in vitro*. MCF-7 cells were seeded in a 96-well plate and given different concentrations of preparations (QR, FT, QR@FT, PEG-CPP30/QR@FT). After incubation for 32 h, the medium was replaced with fresh medium. In the laser group, the 660 nm laser (0.4 W/cm^2) was irradiated for 3 min. All groups continued to be incubated for another 16 h. Finally, 20 μL 5 mg/mL MTT solution was added to each hole for 4 h, and then 100–150 μL DMSO was added. The excitation wavelength was set at 490 nm using an enzyme marker to determine the absorbance of each hole. Cell viability was calculated using formula S3 in the ESM.

4.8 Cell apoptosis study

MCF-7 cells were cultured in 24-well plate for 12 h and given 1 mL fresh cell medium containing different preparations (QR concentration of 50 μg/mL), other operations were consistent with *in vitro* cytotoxicity test. After culture, the cells were digested and washed with PBS. The cells were added with 295 μL Annexin V-FITC binding solution and 5 μL Annexin V-FITC dye solution, incubating for 15 min, then 10 μL PI dye solution was added, and apoptosis detection was completed by flow cytometry within 1 h.

4.9 Cell cycle determination

MCF-7 cells were seeded on the 6-well plate, and given different preparations (with 10 μg/mL QR content). After 24 h of treatment, the cells were collected, added with 1 mL of pre-cooled 70% ethanol and fixed at −20 °C for 36 h. The cells were centrifuged and the

supernatant was discarded. Each sample was incubated in 0.5 mL PI staining solution at 37 °C for 30 min, and detected by flow cytometry subsequently.

4.10 HSP70, HSP90, HSP27 measurement by western blot

To determine the inhibitory effect of NPs on HSPs in phototherapy, MCF-7 cells were inoculated into six-well plates and divided into five groups: control, FT + L, FT + QR + L, QR@FT + L, and PEG-CPP30/QR@FT + L. The protein in each group was extracted by cell lysis, and the target protein bands were obtained by electrophoresis, membrane transfer and other operations. The bands were closed, washed and developed, and the expression levels of target proteins HSP70, HSP90, and HSP27 in each group were finally obtained.

4.11 Animal and tumor-bearing mouse model

All animal study protocols were conducted in accordance with the guidelines approved by the Institutional Animal Care and Use Committee at Beijing University of Chinese Medicine. Balb/C nude mice (4–5 weeks, 20 g) were obtained from Sipeifu Biological Technology Co. Ltd (Beijing, China) and raised under standard conditions. In addition, a breast cancer tumor model was established. MCF-7 cells suspended in PBS were subcutaneously injected in the right side of the mice (1×10^6 cells per mouse). The tumor volume was calculated using formula S4 in the ESM. When the tumor-bearing mouse model was successfully constructed, they could be used for follow-up pharmacodynamic experiments.

4.12 *In vivo* fluorescence imaging and photothermal conversion effect of NPs

In order to explore the *in vivo* targeting of NPs, sodium fluorescein-labeled NPs were injected by tail vein injection into the mice. Fluorescence imaging was performed on mice at 0, 3, 6, 9, 12, and 24 h after administration. The fluorescence were recorded by a Living imaging system (BerthoLd, DE). Finally, the tumors and major organs were dissected for *in vitro* imaging.

Mice were injected with normal saline, FT, QR@FT and PEG-CPP30/QR@FT through the tail vein. 9 h after the administration, the tumor site was irradiated by laser (0.4 W/cm^2, 660 nm), and the temperature of the tumor site was recorded by thermal imaging camera at 0, 1, 2, 3, 5, and 7 min, and then the heating curve was plotted.

4.13 Statistical methods

All experiments were repeated with at least three samples, and the data were expressed as mean ± SD. Statistical analysis was performed using a one-way ANOVA. $^*P < 0.05$ and $^{***}P < 0.001$ were considered to be statistically significant. For the detailed steps of the other experimental operations, please refer to the Electronic Supplementary Material.

Electronic Supplementary Material: Supplementary material (further details of the DAPI measurement, GSH detection, ROS and MMP detection, TCPP release experiment, Fe^{2+} detection, correlation formula and additional data) is available in the online version of this article at https://doi.org/10.26599/NR.2025.94906991.

Acknowledgements

This research was funded by Young Elite Scientists Sponsorship Program by CACM (No. 2021-QNRC2-A03), the Beijing Natural Science Foundation (No. 7202121), and the National Natural Science Foundation of China (No. 81703715).

Data availability

All data needed to support the conclusions in the paper are presented in the manuscript and/or the Electronic Supplementary Material. Additional data related to this paper may be requested from the corresponding author upon request.

Declaration of competing interest

The authors declare that they have no known competing financial interests or personal relationships that could have appeared to influence the work reported in this paper.

Author contribution statement

X. B. Y. and J. N. designed the experiments. R. Y. Z. performed main experiments, analyzed data and wrote the draft of the manuscript. S. L. L., T. T. F., J. H. K., Y. J. D., and R. R. C. supported experiments and data analysis. M. R. C., D. G. Y. and J. L. gave some suggestions and reviewed writing. All authors read and approved the final manuscript.

Informed consent

Not applicable.

Ethics statement

The animal experiments were carried out following the guidelines of the Beijing University of Chinese Medicine Institutional Committee for the Care and Use of Laboratory Animals and were approved by the Committee on Ethical Use of Animals of Beijing University of Chinese Medicine.

Use of AI statement

None.

References

[1] Pillai, S. C.; Borah, A.; Jindal, A.; Jacob, E. M.; Yamamoto, Y.; Kumar, D. S. BioPerine encapsulated nanoformulation for overcoming drug-resistant breast cancers. *Asian J. Pharm. Sci.* **2020**, *15*, 701–712.

[2] Sung, H.; Ferlay, J.; Siegel, R. L.; Laversanne, M.; Soerjomataram, I.; Jemal, A.; Bray, F. Global Cancer Statistics 2020: GLOBOCAN estimates of incidence and mortality worldwide for 36 cancers in 185 countries. *CA Cancer J. Clin.* **2021**, *71*, 209–249.

[3] Li, Y. T.; Jin, J.; Wang, D. W.; Lv, J. W.; Hou, K.; Liu, Y. L.; Chen, C. Y.; Tang, Z. Y. Coordination-responsive drug release inside gold nanorod@metal-organic framework core-shell nanostructures for near-infrared-induced synergistic chemo-photothermal therapy. *Nano Res.* **2018**, *11*, 3294–3305.

[4] Gao, S.; Liu, M.; Liu, D. Z.; Kong, X. R.; Fang, Y. L.; Li, Y. Y.; Wu, H.; Ji, J. B.; Yang, X. Y.; Zhai, G. X. Biomimetic biomineralization nanoplatform-mediated differentiation therapy and phototherapy for cancer stem cell inhibition and antitumor immunity activation. *Asian J. Pharm. Sci.* **2023**, *18*, 100851.

[5] Guo, W. N.; Chen, Z. Z.; Tan, L. F.; Gu, D. E.; Ren, X. L.; Fu, C. H.; Wu, Q.; Meng, X. W. Emerging biocompatible nanoplatforms for the

potential application in diagnosis and therapy of deep tumors. *VIEW* **2022**, *3*, 20200174.

[6] Chong, H.; Liu, X. W.; Fang, S. Y.; Yang, X. F.; Zhang, Y. F.; Wang, T. Y.; Liu, L.; Kan, Y. S.; Zhao, Y. Q.; Fan, H. Y. et al. Organo-Pt^{II} complexes for potent photodynamic inactivation of multi-drug resistant bacteria and the influence of configuration. *Adv. Sci. (Weinh.)* **2024**, *11*, 2306936.

[7] Sun, R.; Ma, W.; Ling, M. J.; Tang, C. H.; Zhong, M.; Dai, J. Y.; Zhu, M. Y.; Cai, X. Z.; Li, G.; Xu, Q. et al. pH-activated nanoplatform for visualized photodynamic and ferroptosis synergistic therapy of tumors. *J. Control Release* **2022**, *350*, 525–537

[8] Hu, X. M.; Zhu, C. J.; Sun, F. W.; Yang, J.; Chen, Z. J.; Ao, H. Y.; Cui, C.; Yang, Z.; Huang, W. Insights into the organic semiconducting photosensitizers for hypoxia-tolerant type I photodynamic therapy. *Nano TransMed* **2022**, *1*, e9130010.

[9] Zhu, J.; Ding, T.; Jin, K. F.; Xing, Y. X.; Huang, J. X.; Xia, D. Q.; Cai, K. Y.; Zhang, J. X. Integrated energy conversion units in nanoscale frameworks induce sustained generation and amplified lethality of singlet oxygen in oxidative therapy of tumor. *VIEW* **2022**, *3*, 20220051.

[10] Lv, J.; Qiu, Y. H.; Pan, L.; Zhang, X. Y.; Li, M. T.; Yin, X. Q. Photothermal/photodynamic antibacterial hydrogel embedded with copper carbon dots and Au nanoparticles. *Nano TransMed* **2024**, *3*, 100034.

[11] Ma, W.; Sun, R.; Tang, L. G.; Li, Z. B.; Lin, L.; Mai, Z.; Chen, G.; Yu, Z. Q. Bioactivable STING nanoagonists to synergize NIR-II mild photothermal therapy primed robust and long-term anticancer immunity. *Adv. Mater.* **2023**, *35*, 2303149.

[12] Yi, X. L.; Duan, Q. Y.; Wu, F. G. Low-temperature photothermal therapy: Strategies and applications. *Research (Wash. D. C)* **2021**, *2021*, 9816594.

[13] Zhang, Z. C.; Ji, Y. T.; Liu, D. F.; Zhou, S. H.; Wang, Z. J.; Chen, R. R.; Li, T.; Zhao, B. X.; Yao, H. T.; Du, M. Q. Heat shock protein inhibitors show synergistic antibacterial effects with photodynamic therapy on caries-related streptococci *in vitro* and *in vivo*. *mSphere* **2023**, *8*, e00679–22.

[14] Chang, M. Y.; Hou, Z. Y.; Wang, M.; Yang, C. Z.; Wang, R. F.; Li, F.; Liu, D. L.; Peng, T. L.; Li, C. X.; Lin, J. Single-atom Pd nanozyme for ferroptosis-boosted mild-temperature photothermal therapy. *Angew Chem., Int. Ed.* **2021**, *60*, 12971–12979.

[15] Marzec, A.; Augusciak-Duma, A.; Kupny-Bujoczek, D.; Witek, L.; Olejek, A.; Gabriel, I. Expression of heat shock proteins HSPA1A, HSPA1B and TP53 in vulval lichen planus and vulval lichen sclerosus. *Ginekol. Pol.* **2023**, *94*, 527–531.

[16] Mazurakova, A.; Solarova, Z.; Koklesova, L.; Caprnda, M.; Prosecky, R.; Khakymov, A.; Baranenko, D.; Kubatka, P.; Mirossay, L.; Kruzliak, P. et al. Heat shock proteins in cancer - Known but always being rediscovered: Their perspectives in cancer immunotherapy. *Adv. Med. Sci.* **2023**, *68*, 464–473.

[17] Zhang, M.; Bi, X. W. Heat shock proteins and breast cancer. *Int. J. Mol. Sci.* **2024**, *25*, 876.

[18] Wu, J. M.; Liu, T. E.; Rios, Z.; Mei, Q. B.; Lin, X. K.; Cao, S. S. Heat shock proteins and cancer. *Trends Pharmacol. Sci.* **2017**, *38*, 226–256.

[19] Shi, X. L.; Zhu, Q. Determination of Apigenin, Quercetin and asterone in aster from different places by HPLC wavelength switching. *Pharmaceut. Chem.* **2022**, *48*, 184–186.

[20] Zhou, A. HPLC method was used to determine the contents of xanthophyllin, citipine and quercetin in Gleditsia sinensis from different regions. *J. China Prescript. Drug* **2022**, *20*, 26–28.

[21] Li, X.; Xu, X.; Xu, J.; Guo, G. B.; Li, X. X.; Lin, J.; Zhang, T. J.; Liu, M. Study on the quality markers of Panax Notoginseng powder based on its function of promoting blood circulation. *Modernizat. Tradit. Chin. Med. Mater. Med. World Sci. Technol.* **2022**, *24*, 35–46.

[22] Cui, X. M.; Zhang, F.; Zhao, Y. Y.; Li, P.; Wang, T.; Xu, Z. L.; Zhang, J. J.; Zhang, W. F. A novel ligand-modified nanocomposite microparticles improved efficiency of quercetin and paclitaxel delivery in the non-small cell lung cancer. *Drug Deliv.* **2022**, *29*, 3123–3133.

[23] Maugeri, A.; Calderaro, A.; Patanè, G. T.; Navarra, M.; Barreca, D.; Cirmi, S.; Felice, M. R. Targets involved in the anti-cancer activity of quercetin in breast, colorectal and liver neoplasms. *Int. J. Mol. Sci.* **2023**, *24*, 2952.

[24] Sethi, G.; Rath, P.; Chauhan, A.; Ranjan, A.; Choudhary, R.; Ramniwas, S.; Sak, K.; Aggarwal, D.; Rani, I.; Tuli, H. S. Apoptotic mechanisms of quercetin in liver cancer: Recent trends and advancements. *Pharmaceutics* **2023**, *15*, 712.

[25] Ruidas, B.; Sur, T. K.; Das Mukhopadhyay, C.; Sinha, K.; Som Chaudhury, S.; Sharma, P.; Bhowmick, S.; Majumder, R.; Saha, A. Quercetin: A silent retarder of fatty acid oxidation in breast cancer metastasis through steering of mitochondrial CPT1. *Breast Cancer* **2022**, *29*, 748–760.

[26] Sundaram, M. K.; Raina, R.; Afroze, N.; Bajbouj, K.; Hamad, M.; Haque, S.; Hussain, A. Quercetin modulates signaling pathways and induces apoptosis in cervical cancer cells. *Biosci. Rep.* **2019**, *39*, BSR20190720.

[27] Zhao, X.; Wang, Q. T.; Yang, S. J.; Chen, C.; Li, X. Y.; Liu, J. Y.; Zou, Z. M.; Cai, D. Y. Quercetin inhibits angiogenesis by targeting calcineurin in the Xenograft model of human breast cancer. *Eur. J. Pharmacol.* **2016**, *781*, 60–68.

[28] Feng, L.; Yang, J. M.; Yang, R.; Sun, L.; Dong, L. L.; Zhang, Q. W. Study on reversal effect of quercetin on human cervical squamous carcinoma cisplatin-resistant cell line SiHa/DDP. *China Pharmacy* **2021**, *32*, 2875–2879.

[29] Gao, P.; Wang, H.; Cheng, Y. Y. Strategies for efficient photothermal therapy at mild temperatures: Progresses and challenges. *Chin. Chem. Lett.* **2022**, *33*, 575–586.

[30] Tian, H. L.; Zhang, J.; Zhang, H. Y.; Jiang, Y.; Song, A. X.; Luan, Y. X. Low side-effect and heat-shock protein-inhibited chemo-phototherapy nanoplatform via co-assembling strategy of Biotin-tailored IR780 and quercetin. *Chem. Eng. J.* **2020**, *382*, 123043.

[31] Bangar, S. P.; Chaudhary, V.; Sharma, N.; Bansal, V.; Ozogul, F.; Lorenzo, J. M. Kaempferol: A flavonoid with wider biological activities and its applications. *Crit. Rev. Food Sci. Nutr.* **2023**, *63*, 9580–9604.

[32] Kandemir, K.; Tomas, M.; McClements, D. J.; Capanoglu, E. Recent advances on the improvement of quercetin bioavailability. *Trends Food Sci. Technol.* **2022**, *119*, 192–200.

[33] Xiong, Q.; Wang, Y. W.; Wan, J. Y.; Yuan, P.; Chen, H. L.; Zhang, L. K. Facile preparation of hyaluronic acid-based quercetin nanoformulation for targeted tumor therapy. *Int. J. Biol. Macromol.* **2020**, *147*, 937–945.

[34] Huang, C. Y.; Chen, T. K.; Zhu, D. M.; Huang, Q. Q. Enhanced tumor targeting and radiotherapy by quercetin loaded biomimetic nanoparticles. *Front. Chem.* **2020**, *8*, 225.

[35] Wang, B. H.; Ma, Y. N.; Xu, W. F.; Tang, K. W. Cr-Based MOF for efficient adsorption of Au at low concentrations. *Langmuir* **2022**, *38*, 8954–8963.

[36] Li, Y. W.; Yang, R. T. Gas adsorption and storage in metal-organic framework MOF-177. *Langmuir* **2007**, *23*, 12937–12944.

[37] Xu, X. F.; Deng, Q. M.; Chen, H. C.; Humayun, M.; Duan, D. L.; Zhang, X.; Sun, H. C.; Ao, X.; Xue, X. Y.; Nikiforov, A. et al. Metal-organic frameworks offering tunable binary active sites toward highly efficient urea oxidation electrolysis. *Research* **2022**, *2022*, 9837109.

[38] Giménez-Marqués, M.; Hidalgo, T.; Serre, C.; Horcajada, P. Nanostructured metal-organic frameworks and their Bio-related applications. *Coord. Chem. Rev.* **2016**, *307*, 342–360.

[39] Yang, J.; Dai, D. H.; Zhang, X.; Teng, L. S.; Ma, L. J.; Yang, Y. W. Multifunctional metal-organic framework (MOF)-based nanoplatforms for cancer therapy: From single to combination therapy. *Theranostics* **2023**, *13*, 295–323.

[40] Coluccia, M.; Parisse, V.; Guglielmi, P.; Giannini, G.; Secci, D. Metal-

organic frameworks (MOFs) as biomolecules drug delivery systems for anticancer purposes. *Eur. J. Med. Chem.* **2022**, *244*, 114801.

[41] Yao, H.; Wang, F. F.; Chong, H.; Wang, J. J.; Bai, Y.; Du, M.; Yuan, X. H.; Yang, X. F.; Wu, M.; Li, Y. P. et al. A curcumin-modified coordination polymers with ROS scavenging and macrophage phenotype regulating properties for efficient ulcerative colitis treatment. *Adv. Sci. (Weinh.)* **2023**, *10*, 2300601.

[42] Wan, X. Y.; Zhong, H.; Pan, W.; Li, Y. H.; Chen, Y. Y.; Li, N.; Tang, B. Programmed release of dihydroartemisinin for synergistic cancer therapy using a $CaCO_3$ mineralized metal-organic framework. *Angew. Chem., Int. Ed.* **2019**, *58*, 14134–14139.

[43] Kondo, E.; Saito, K.; Tashiro, Y.; Kamide, K.; Uno, S.; Furuya, T.; Mashita, M.; Nakajima, K.; Tsumuraya, T.; Kobayashi, N. et al. Tumour lineage-homing cell-penetrating peptides as anticancer molecular delivery systems. *Nat. Commun.* **2012**, *3*, 951.

[44] Gao, Y. Y.; Yang, R. Q.; Lou, K. L.; Dang, Y. Y.; Dong, Y. Y.; He, Y. Y.; Huang, W. H.; Chen, M.; Zhang, G. J. *In vivo* visualization of fluorescence reflecting CDK4 activity in a breast cancer mouse model. *MedComm* **2022**, *3*, e136.

[45] Kıyga, E.; Şengelen, A.; Adıgüzel, Z.; Uçar, E. Ö. Investigation of the role of quercetin as a heat shock protein inhibitor on apoptosis in human breast cancer cells. *Mol. Biol. Rep.* **2020**, *47*, 4957–4967.

[46] Yin, D.; Cao, J. Y.; Yang, Y.; Li, Z. T.; Liu, H.; Tang, T. T.; Ni, W. J.; Zhang, Y. L.; Jiang, W.; Wen, Y. et al. Quercetin alleviates tubulointerstitial inflammation by inhibiting exosomes-mediated crosstalk between tubular epithelial cells and macrophages. *Inflamm. Res.* **2023**, *72*, 1051–1067.

[47] Sang, D. P.; Li, R. J.; Lan, Q. Quercetin sensitizes human glioblastoma cells to temozolomide *in vitro* via inhibition of Hsp27. *Acta Pharmacol. Sin.* **2014**, *35*, 832–838.

[48] Pan, W. L.; Tan, Y.; Meng, W.; Huang, N. H.; Zhao, Y. B.; Yu, Z. Q.; Huang, Z.; Zhang, W. H.; Sun, B.; Chen, J. X. Microenvironment-driven sequential ferroptosis, photodynamic therapy, and chemotherapy for targeted breast cancer therapy by a cancer-cell-membrane-coated nanoscale metal-organic framework. *Biomaterials* **2022**, *283*, 121449.

[49] Yu, D. L.; Zha, Y.; Zhong, Z.; Ruan, Y. M.; Li, Z. W.; Sun, L. L.; Hou, S. Improved detection of reactive oxygen species by DCFH-DA: New insight into self-amplification of fluorescence signal by light irradiation. *Sensors Actuat. B Chem.* **2021**, *339*, 129878.

[50] Małota, K.; Student, S.; Świątek, P. Low mitochondrial activity within developing earthworm male germ-line cysts revealed by JC-1. *Mitochondrion.* **2019**, *44*, 111–121.

[51] Kong, Q. C.; Sun, W. Y.; Lin, J. Y.; Wang, L.; Dong, B. Research progress of photodynamic therapy based on porphyrin-metal organic framework materials. *Chin. J. Lumin.* **2023**, *44*, 1505–1519.

[52] Xu, D. X.; Duan, Q.; Yu, H.; Dong, W. Y. Photodynamic therapy based on porphyrin-based metal-organic frameworks. *J. Mater. Chem. B* **2023**, *11*, 5976–5989.

[53] Peng, X. J.; Xu, L.; Zeng, M.; Dang, H. Application and development prospect of nanoscale iron based metal-organic frameworks in biomedicine. *Int. J. Nanomed.* **2023**, *18*, 4907–4931.

[54] Hu, H. L.; Dai, Z. C.; Zhang, F. F.; Xin, C. L.; An, Q.; Meng, X. Y.; Hu, Z. F.; Wang, W. J.; Tian, L.; Zheng, X. W. Metal organic frameworks based intelligent nanoadjuvants for boosting tumor immunotherapy through enhanced ICD and lactic acid regulation. *Chem. Eng. J.* **2024**, *479*, 147464.

[55] Zhang, Q. F.; Kuang, G. Z.; Wang, H. B.; Zhao, Y. J.; Wei, J.; Shang, L. R. Multi-bioinspired MOF delivery systems from microfluidics for tumor multimodal therapy. *Adv. Sci. (Weinh.)* **2023**, *10*, 2303818.

[56] Goji, N.; Ramezani, M.; Saljooghi, A. S.; Alibolandi, M. Porphyrin-based metal-organic frameworks: Focus on diagnostic and therapeutic applications. *J. Nanostructure Chem.* **2024**, *14*, 167–208.

[57] Sun, J. M.; Jiang, K.; Wang, Y. F.; Liu, Y. Q.; Wang, T.; Ding, S. Y.; Zhang, X. Z.; Xiong, W. W.; Zheng, F. F.; Yang, H. T. et al. One-pot synthesis of tumor-microenvironment responsive degradable nanoflower-medicine for multimodal cancer therapy with reinvigorating antitumor immunity. *Adv. Healthc. Mater.* **2023**, *12*, 2302016.

[58] Sabzehmeidani, M. M.; Kazemzad, M. Recent advances in surface-mounted metal-organic framework thin film coatings for biomaterials and medical applications: A review. *Biomater. Res.* **2023**, *27*, 115.

[59] Wang, B. Tumor Microenvironment responsive porphyrin-metal coordination polymers nanoparticles: Synthesis and their application in tumor thersnostics. Master Degree Thesis, Nanjing University of Posts and Telecommunications, Nanjing, 2021.

This is an open access article under the terms of the Creative Commons Attribution 4.0 International License (CC BY 4.0, https://creativecommons.org/licenses/by/4.0/).

© The Author(s) 2025. Published by Tsinghua University Press.